Co-Fe-P nanosheet arrays as highly synergistic and active electrocatalyst for oxygen evolution reaction

Yanyu Xie, Huanfeng Huang, Zhuodi Chen, Zhujie He, Zhixiang Huang, Shunlian Ning, Yanan Fan, Mihail Barboiu, Jian-Ying Shi, Dawei Wang, et al.

▶ **To cite this version:**

Yanyu Xie, Huanfeng Huang, Zhuodi Chen, Zhujie He, Zhixiang Huang, et al.. Co-Fe-P nanosheet arrays as highly synergistic and active electrocatalyst for oxygen evolution reaction. Inorganic Chemistry, 2022, 61 (21), pp.8283-8290. 10.1021/acs.inorgchem.2c00727 . hal-03749340

HAL Id: hal-03749340
https://hal.science/hal-03749340

Submitted on 10 Aug 2022

HAL is a multi-disciplinary open access archive for the deposit and dissemination of scientific research documents, whether they are published or not. The documents may come from teaching and research institutions in France or abroad, or from public or private research centers.

L'archive ouverte pluridisciplinaire **HAL**, est destinée au dépôt et à la diffusion de documents scientifiques de niveau recherche, publiés ou non, émanant des établissements d'enseignement et de recherche français ou étrangers, des laboratoires publics ou privés.

Co-Fe-P nanosheet arrays as highly synergistic and active electrocatalyst for oxygen evolution reaction

Yanyu Xie[a], Huanfeng Huang[a], Zhuodi Chen[a], Zhujie He[a], Zhixiang Huang[a], Shunlian Ning[a], Yanan Fan[a], Mihail-Dumitru Barboiu[a, b], Jian-Ying Shi[a], Dawei Wang[a]* and Cheng-Yong Su[a]

[a] Y. Xie, H. Huang, Z. Chen, Z. He, Z. Huang, S. Ning, Y. Fan, Prof. M.-D. Barboiu, Prof. J.-Y. Shi, Prof. D. Wang* and Prof. C.-Y. Su

Lehn Institute of Functional Materials

MOE Laboratory of Bioinorganic and Synthetic Chemistry

School of Chemistry

Sun Yat-Sen University

Guangzhou 510275, China.

E-mail: wdawei@mail.sysu.edu.cn

[b] Prof. M.-D. Barboiu

Institut Europeen des Membranes

Adaptive Supramolecular Nanosystems Group

University of Montpellier

ENSCM-CNRS, Pl. E.Bataillon CC047, Montpellier 34095, France

Supporting information for this article can be found under:

https://doi.org/xx.xxxx/chem.xxxxxxxxx.Supporting information for this article can be found under:

https://doi.org/xx.xxxx/chem.xxxxxxxxx.

Abstract: The rational design and synthesis of highly active electrocatalysts for oxygen evolution reaction (OER) is of critical importance to the large-scale production of hydrogen by water electrolysis. Here, we develop a bimetallic, synergistic, and highly efficient Co-Fe-P electrocatalyst for OER, by selecting a two-dimensional MOF of Co-ZIF-L as the precursor. The Co-Fe-P electrocatalyst features pronounced synergistic effect induced by notable electron transfer from Co to Fe, and large electrochemical active surface area (ECSA) achieved by organizing the synergistic Co-Fe-P into hierarchical nanosheet arrays with disordered Co-P/Fe-P grain boundary. Such features facilitate the generation of abundant and

efficiently exposed Co^{3+} sites for electrocatalytic OER, and thus enable the Co-Fe-P to deliver excellent activity (overpotential and Tafel slope as low as 240 mV and 36 mV dec^{-1}, respectively, at a current density of 10 mA cm^{-2} in 1.0 M KOH solution). The Co-Fe-P electrocatalyst also shows great durability by steadily working for up to 24 h. Our work thus provides new insight into the development of highly efficient electrocatalysts based on nanoscale and/or electronic structure engineering.

Introduction

As a green and recycle energy source, hydrogen (H_2) has been regarded as a promising solution to the global concern over ever-growing energy crisis and environmental pollution.[1, 2] Water electrolysis is an important technique to produce hydrogen.[3] The large-scale application of water electrolysis, however, is usually restricted by the anodic half reaction, that is, oxygen evolution reaction (OER).[3-5] The OER is a four-electron procedure that requires high overpotential and results in sluggish kinetics and unsatisfying efficiency of the overall water hydrolysis process.[4-7] Therefore, a series of transitional metal compounds (Co, Ni, Fe, etc.) including oxides, sulfides and phosphides has been developed as inexpensive yet efficient electrocatalysts so as to lowering the overpotential and accelerate the kinetics of OER.[8-12] Among these transitional metal compounds, transitional metal phosphides (TMPs) have been widely investigated due to their excellent electrocatalytic properties, which are close or even superior to RuO_2, one of typical and commercially available OER electrocatalysts.[12-16] In recent years, TMPs derived from metal-organic frameworks (MOFs) have attracted particular research interest, since the MOFs-derived TMPs usually possess highly porous structure, rich structural diversity, and tunable composition that are beneficial to the design and synthesis of active OER electrocatalysts. [17-21]

When serving as OER catalysts, bimetallic catalysts often show better performance than their monometallic counterparts due to their optimized electronic structure and synergistic effect.[22-27] For example, Co can be coupled with Fe, Zn, or Ni to enhance its electrocatalytic activity, since the coupling of a second metal facilitates the generation of abundant high-valence Co species (Co^{3+} and/or Co^{4+}), the highly

active sites for electrocatalytic OER.[22, 23, 26, 28, 29] In this regard, bimetallic TMPs, especially those derived from MOFs, are of particular interest to construct highly active OER electrocatalyst, since their highly porous structure inherited from MOFs could further facilitate the efficient exposure of catalytic sites with synergistic effects.[30-33]

Here, we design and synthesize a Co- and Fe-based bimetallic phosphide (denoted as Co-Fe-P; Figure 1a), using a two-dimensional Fe-doped Co-MOFs as the precursor. The bimetallic Co-Fe-P electrocatalyst features pronounced synergistic effect induced by notable electron transfer from Co to Fe, and large electrochemical active surface area (ECSA) achieved by organizing the synergistic Co-F-P into hierarchical nanosheet arrays with disordered grain boundary between neighboring Co-P and Fe-P. Benefitting from such pronounced synergistic effect and large ECSA, the bimetallic Co-Fe-P electrocatalyst with abundant and efficiently exposed high-valence Co^{3+} shows excellent activity and stability towards OER, comparable or even superior to the best Co-Fe-based bimetallic electrocatalysts developed so far. When evaluated in 1.0 M KOH solution, the bimetallic Co-Fe-P electrocatalyst requires only a low overpotential of 240 mV and a small Tafel slope of 36 mV dec^{-1} to drive a current density of 10 mA cm^{-2}, and is capable of working steadily for 24 h.

Results and Discussion

Co-ZIF-L, a MOF with two-dimensional layered structure constructed from Co^{2+} and 2-methylimidazole, was synthesized according to a previously reported procedure and selected as the precursor.[34-36] The leaf-like nanosheets of Co-ZIF-L with a length of about 5 μm and a thickness of about 20 nm were grown on carbon cloth (CC) to form dense packing arrays, as shown in the scanning electron microscopes (SEM) images in Figure 1b and Figure S1 in the Supporting Information. Each Co-ZIF-L nanosheet show smooth surface and sharp crystal boundary, and its powder X-ray diffraction (PXRD) pattern matches well with the simulated one (Figure S2), indicating the high crystallinity of Co-ZIF-L nanosheet.

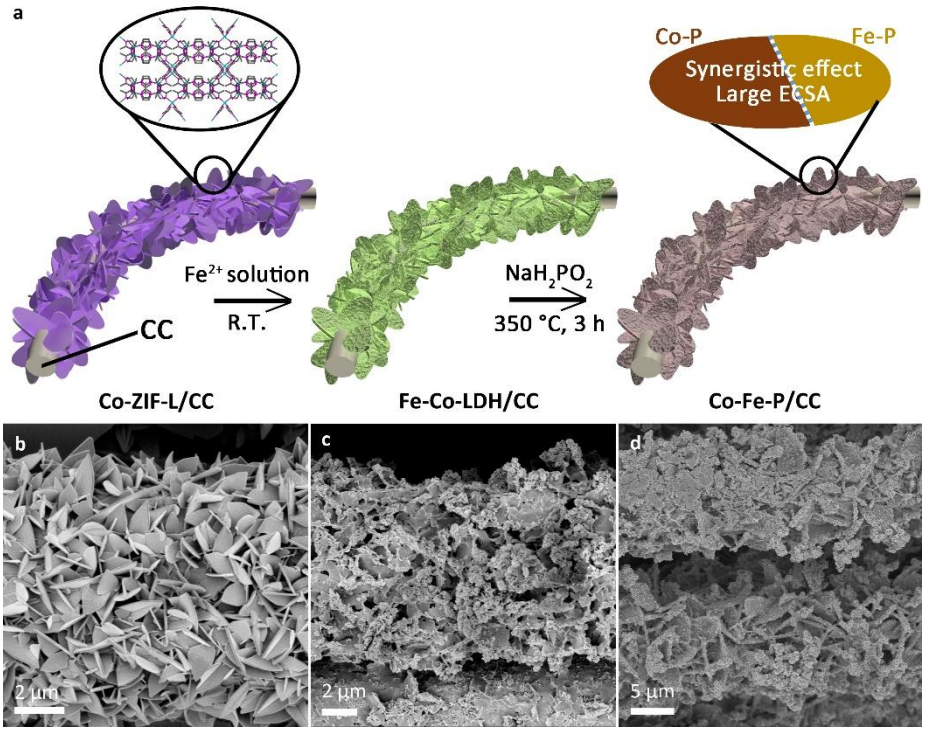

Figure 1. (a) Schematic illustration of the synthesis of Co-Fe-P/CC. SEM images of (b) Co-ZIF-L/CC, (c) Co-Fe-LDH/CC, and (d) Co-Fe-P/CC.

The CC-supported Co-ZIF-L nanosheet arrays (denoted as Co-ZIF-L/CC) were treated in an aqueous solution of Fe^{2+} at room temperature to convert Co-ZIF-L into a layer-double hydroxide of Co and Fe (denoted as Co-Fe-LDH, Figure 1a).[35, 37, 38] Each Co-Fe-LDH nanosheet shows rough surface, due to the in-situ formation of a large number of much smaller, secondary nanosheets (Figure S3). The doping of Fe in the resulted Co-Fe-LDH was confirmed by energy-dispersive X-ray spectroscopy (EDX) result, which revealed a Fe:Co atomic ratio of about 1.8:1 (Table S1). The formation of Co-Fe-LDH was examined and verified by transmission electron microscopy (TEM) images (Figure S4-S6), which showed lattice fringes, diffraction rings, and selected area electron diffraction (SAED) pattern that all can be ascribed to the (110) and (012) planes of Co-Fe-LDH. [39, 40] In addition, the PXRD pattern of the resulted nanosheets exhibits peaks at 10.1°, 20.4°, 34.3° and 60.8° that can also be assigned to the (003), (006), (012) and (110) plane of Co-Fe-LDH (Figure S7), respectively, and no peaks of the Co-ZIF-L precursors can be found. The above results from EDX, TEM, SAED and PXRD thus collectively confirm that the resulted nanosheets consist of Co-Fe-LDH and the conversion of Co-ZIF-L into Co-Fe-LDH is completed.

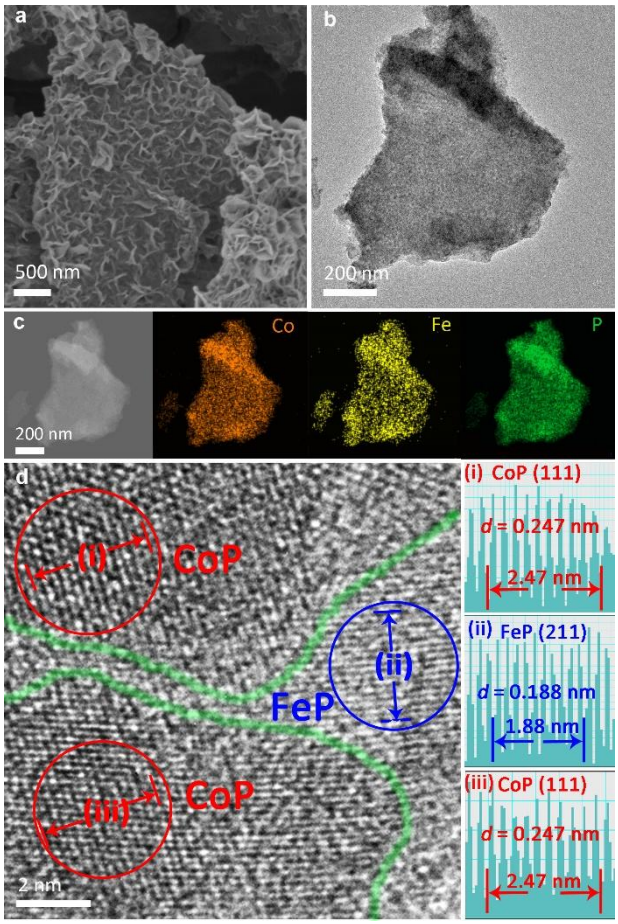

Figure 2. Electron microscopy images of Co-Fe-P nanosheets. (a) SEM, (b) TEM, (c) EDS elemental maps, and (d) HRTEM.

The Co-Fe-LDH nanosheet arrays was then converted into active OER electrocatalyst by phosphorization (Figure 1a). Although the phosphorized Co-Fe-LDH (denoted as Co-Fe-P) nanosheets do not change significantly in overall morphology and structure (Figure 1d and 2a), their structure becomes quite different (Figure 2b). The EDX element maps of Co-Fe-P nanosheets indicate a uniform distribution of Co, Fe and P (Figure 2c), and thus suggest the successful phosphorization of Fe and Co in Co-Fe-LDH. Furthermore, high-resolution TEM (HRTEM) image in Figure 2d manifests two new sets of lattice spacing, in which 0.188 nm corresponds to the (211) interplanar spacing of orthorhombic Fe-P (JCPDS #78-1443) and 0.247 nm corresponds to the (111) interplanar spacing of orthorhombic Co-P (JCPDS#29-0497). From the HRTEM image, grain boundaries with less order structure are also observed between neighboring Co-P and Fe-P, which is likely due to the structural mismatch (cf. Figure 3a) and interface defects between Co-P and Fe-P. The SAED pattern of

Co-Fe-P nanosheets also presents concentric rings that can be assigned to the (211) and (111) planes (Figure S8). Moreover, the PXRD pattern of Co-Fe-P shows several broad peaks due to the overlap of adjacent peaks of Co-P and Fe-P (Figure 3a); however, the existence of Co-P and Fe-P can still be distinguished and confirmed by the peaks located at 34.0 and 52.2°, which correspond the (200) plane of Fe-P and the (103) plane of Co-P, respectively. Quantitatively, the Fe:Co:P atomic ratio is determined to be about 1.5:1:2.5 based on the EDX data shown in Figure S9 and Table S2. The above results thus show that the Co-Fe-P consists of Co-P and Fe-P that organize in a hierarchical structure of CC-supported nanosheet arrays. Such hierarchical structure could effectively facilitate the exposure of electrocatalytic sites in each Co-Fe-P nanosheet and also well isolate the Co-Fe-P nanosheets from each other, thus imparting the Co-Fe-P electrocatalyst with excellent activity and stability for OER (cf. Figure 4 and related discussion therein).

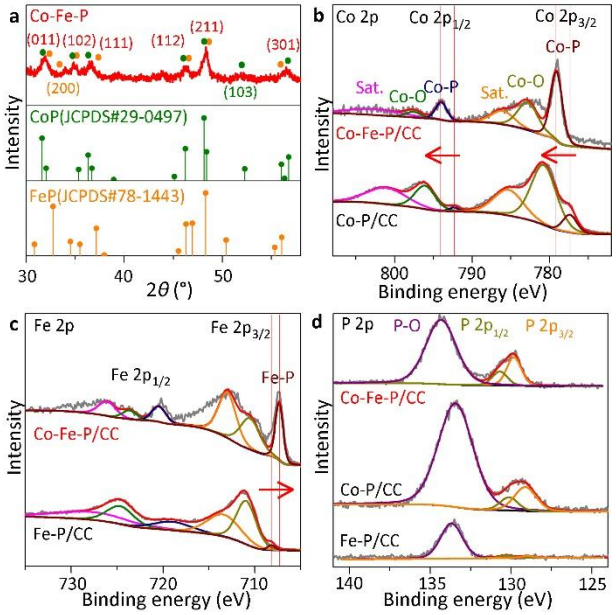

Figure 3. (a) XRD patterns and (b-d) XPS spectra of Co-Fe-P. (b) Co 2p, (c) Fe 2p, and (d) P 2p.

The surface elemental composition and valence state of Co-Fe-P/CC was probed by X-ray photoelectron spectroscopy (XPS). The full XPS survey confirms the presence of C, P, Co and Fe in Co-Fe-P/CC (Figure S10). O is also found in the XPS spectrum of Co-Fe-P/CC, which is a commonly reported phenomenon induced by the oxidation of active Co-P and Fe-P by atmospheric oxygen under ambient

condition.[30, 31, 41] The Co 2p spectrum is deconvoluted into peaks of Co-O at 796.9 eV, Co-P at 794.0 and 779.0 eV, and their satellite peaks at 802.8 and 784.9 eV, respectively (Figure 3b); the P 2p spectrum is deconvoluted into peaks of P $2p_{1/2}$ at 130.7 eV, P $2p_{3/2}$ at 129.8 eV and P-O at 134.3 eV (Figure 3d). The peak of Co-P (794.0 and 779.0 eV) and Fe-P (707.4 eV) confirm the existence of Co-P and Fe-P in Co-Fe-P/CC. The peaks corresponding to P-O, Co-O and Fe-O bonds indicates that Co-Fe-P is prone to oxidation by atmosphere oxygen under ambient condition, which is due to the active chemical properties of Co-P and Fe-P.[30, 31, 41] Moreover, as compared with the spectra of with Co-P/CC and Fe-P/CC (Figure 3d; also see their XRD patterns and SEM images in Figure S11-S13), the XPS spectra of Co-Fe-P/CC show a positive shift of 0.6 eV in the Co-P peak position, and a negative shift of 0.8 eV in the Fe-P peak position, which thus clearly indicates the electron transfer from Co to Fe in Co-Fe-P and the synergistic effects between Co and Fe. Such electron transfer from Co to Fe leads to the generation of more Co^{3+} in high-valence state (cf. Figure 5a and related discussion therein), and thus is expected to induced better OER performance when use Co-Fe-P for electrocatalytic water splitting, since high-valence-state Co (particularly, Co^{3+} and/or Co^{4+}) has been demonstrated to be the catalytic species of OER.[26, 28, 32]

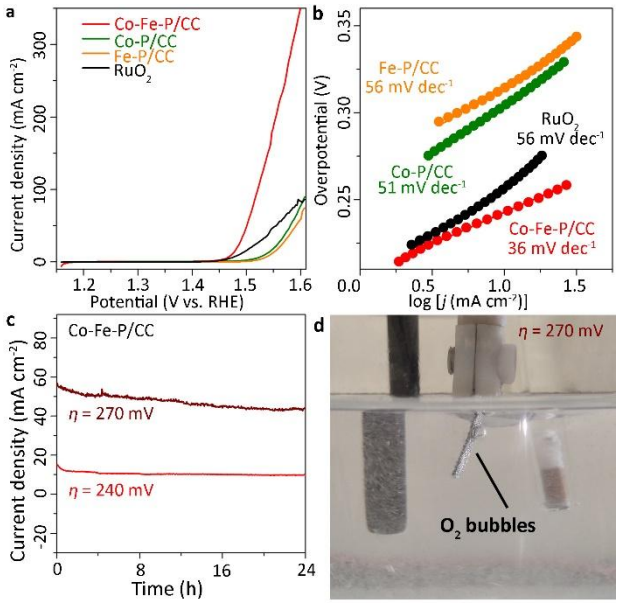

Figure 4. Electrocatalytic activity of Co-Fe-P/CC, Co-P/CC and Fe-P/CC towards OER evaluated in the aqueous solution of 1.0 M KOH. (a) Polarization curves, (b) Tafel plots, (c) *i-t* curves at static overpotential of 240 and 270 mV for 24 h for Co-Fe-P/CC, (d) Optical image showing the OER process.

The electrocatalytic OER activity of Co-Fe-P/CC was evaluated in a three-electrode electrochemical cell with alkaline electrolyte (aqueous solution of 1.0 M KOH). The polarization curves obtained from linear scanning voltammetry (LSV) in Figure 4a reveal the excellent electrocatalytic activity of Co-Fe-P/CC, which only needs an overpotential of 240 mV to reach a current density of 10 mA cm^{-2}. To obtain the same current density, Co-P/CC, Fe-P/CC and the commercially available benchmark catalyst of RuO_2 need much higher overpotential of 290, 310 and 270 mV, respectively. Moreover, at a higher overpotential of 290 mV, Co-Fe-P/CC is capable of driving a large current density of 100 mA cm^{-2} while much lower current density of 6, 3, and 28 mA cm^{-2} is achieved for Co-P/CC, Fe-P/CC and RuO_2, respectively. The catalytic kinetics was further evaluated based on Tafel plot (Figure 4b). As expected, Co-Fe-P/CC shows much lower Tafel (36 mV dec^{-1}) than that of Co-P/CC (56 mV dec^{-1}), Fe-P/CC (51 mV dec^{-1}) and RuO_2 (56 mV dec^{-1}). The great overpotential and Tafel slope differences between Co-Fe-P/CC, Co-P/CC and RuO_2 indicate that Co-Fe-P/CC can dramatically accelerate the OER kinetics and thus deliver excellent electrocatalytic activity. In fact, as shown in Table S3 in the Supporting Information, the electrocatalytic performance of Co-Fe-P/CC towards OER is comparable or even superior to the best Co-Fe-based bimetallic electrocatalysts developed recently. The electrochemical stability of Co-Fe-P/CC was also tested using constant potential hydrolysis (CPH) method. The Co-Fe-P/CC is able to maintain a current density of 10 mA cm^{-2} steadily for over 24 h at a constant potential at 1.47 V vs. RHE (reversible hydrogen electrode; equivalent to an overpotential of 240 mV; Figure 4c). Even at 1.5 V vs. RHE (overpotential of 270 mV), the current density (50 mA cm^{-2}) does not change significantly after 24 h. The excellent durability of Co-Fe-P/CC is also supported by the experimental observation of vigorous bubbles released from the electrode surface after 24 h of OER process (Figure 4d). The SEM image of Co-Fe-P/CC after 24 h of CPH test is shown in Figure S14, which displays no significant exfoliation or morphology change of the Co-Fe-P nanosheet arrays (cf. Figure 1d, the SEM image of Co-Fe-P nanosheet arrays before CPH test), further demonstrating the excellent structural stability of Co-Fe-P/CC nanosheet arrays.

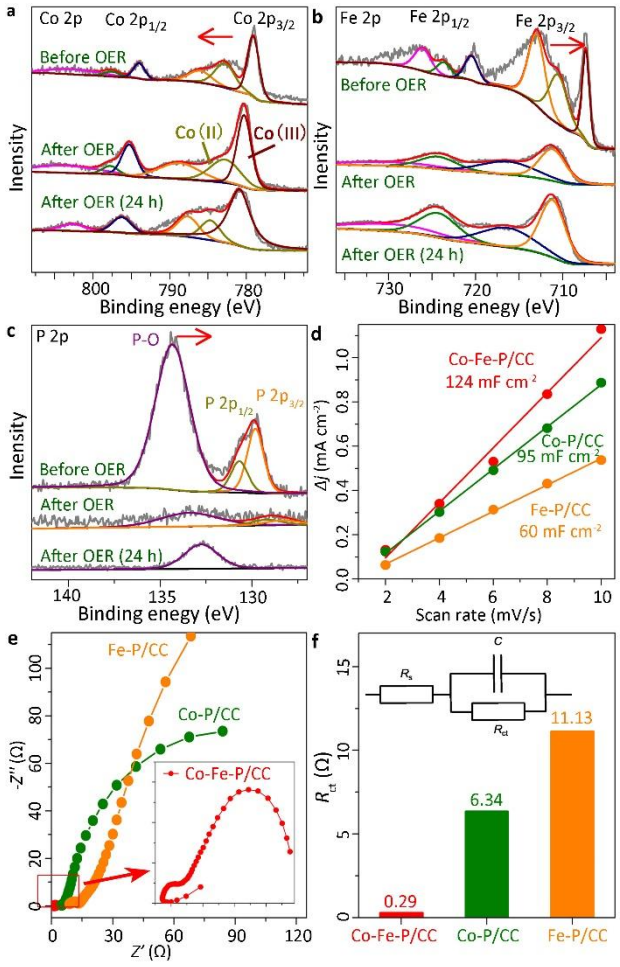

Figure 5. (a-c) High-resolution XPS spectra of (a) Co 2p, (b) Fe 2p and (c) P 2p of Co-Fe-P/CC before and after OER test. (d) Simulated plots of C_{dl}, (e) EIS plots, and (f) R_{ct} fitting result of Co-Fe-P/CC, Co-P/CC and Fe-P/CC evaluated in the solution of 1.0 M KOH (Insert in f is the equivalent circuits).

To rationalize the electrocatalytic activity of Co-Fe-P/CC, the XPS spectra of Co-Fe-P/CC after OER process were collected (Figure 5a-c). As we discussed earlier (cf. Figure 3b-d), synergistic effect induced by the electron transfer from Fe to Co exists in bimetallic Co-Fe-P, and leads to the generation of more Co^{3+} that is beneficial to the electrocatalytic OER performance of Co-Fe-P/CC. Interestingly, further electron transfer and enhanced synergistic effect is observed by comparing the Co-Fe-P/CC before and after OER. After OER, the binding energy of Co 2p further increases, while the binding energy of Fe 2p and P 2p further decreases. Quantitative calculation based on Figure 5a reveals that the Co^{3+}:Co^{2+} ratio increases notably from 1.5 (before OER) to 4.2 (after OER), and thus indicates an outstanding

capability of generating abundant high-valence Co^{3+} during OER process. With so many high-valence Co^{3+} as the active sites, the Co-Fe-P/CC is therefore able to drive the OER process at very low overpotential and Tafel slope.[22, 26] This result clearly demonstrates the great significance and advantage of synergistic effect for the design and synthesis of highly efficient OER electrocatalysts.

Additional characterization techniques were utilized to gain more insights into the excellent electrocatalytic activity of Co-Fe-P/CC. Cyclic voltammetry (CV) at different scan rates was employed to calculate the double layer capacitances (C_{dl}) and ECSA (Figure 5d, and Figure S15-S17). Co-Fe-P/CC exhibits a much higher C_{dl} of 124 mF cm^{-2} than that of the monometallic Co-P/CC (95 mF cm^{-2}) and Fe-P/CC (60 mF cm^{-2}), which indicates that more catalytically active sites are exposed in bimetallic Co-Fe-P/CC for fast OER kinetics. Together with the synergistic effect, the efficient exposure of abundant active sites also could decrease the adsorption energies of reactive species.[22, 31, 42] The higher C_{dl} and ECSA of Co-Fe-P/CC is likely attributed to (1) the hierarchical structure of nanosheet arrays that are capable of efficient exposure of active sites, and (2) the less ordered grain boundary induced by structural mismatch and interface defects between neighboring Co-P and Fe-P, since the appearance of interface disorder/mismatch/defects usually results in more exposed sites and increased surface area.[34, 43, 44] Electro impendence spectrum (EIS) and its derived Nyquist plots, equivalent circuits and fitted data (Figure 5e and 5f) were also collected to analyze the charge transfer behavior of Co-Fe-P/CC. The charge transfer resistance (R_{ct} = 0.29 ohm) of Co-Fe-P/CC is much lower than that of monometallic Co-P/CC (6.34 ohm) and Fe-P/CC (11.13 ohm), suggesting that a much faster charge transfer process and reaction kinetics can be achieved by bimetallic Co-Fe-P/CC. The lower R_{ct} of Co-Fe-P/CC is probably due to the synergistic effect between Co and Fe, which produces more active sites and thus acerates the electron transfers at the catalyst−electrolyte interface.[33, 45, 46] The neighboring arrangement of Co-P and Fe-P in bimetallic Co-Fe-P (Figure 2d) may also play an important in the lower R_{ct} , which could facilitate the electron interaction and induce notable electron transfer at the interface between Co and Fe.

Conclusion

In summary, Co-Fe-P bimetallic nanosheet arrays have been developed as a highly active OER electrocatalyst by Fe-doping and subsequent phosphorization of a two-dimensional MOF, Co-ZIF-L. The doping of Fe induces synergistic effect that enables the generation of abundant high-valence Co^{3+} with great catalytic activity. The hierarchical structure of Co-Fe-P nanosheet arrays with disordered Co-P/Fe-P grain boundary results in large ECSA that facilitates the efficient exposure of catalytic sites. The bimetallic, synergistic Co-Fe-P nanosheet arrays thus deliver excellent activity when used as OER electrocatalyst (overpotential and Tafel slope as low as 240 mV and 36 mV dec^{-1}, respectively, at a current density of 10 mA cm^{-2}), as well as great durability (stead operation for up to 24 h). Our work may inspire the development of highly efficient electrocatalysts by rational engineering of the nanoscale and/or electronic structure of the electrocatalysts.

Experimental Section

Chemicals. Cobalt nitrate hexahydrate ($Co(NO_3)_2 \cdot 6H_2O$), 2-methylimidazole (2-mIm), iron (II) sulfate heptahydrate ($FeSO_4 \cdot 7H_2O$), cobaltous sulfate heptahydrate ($CoSO_4 \cdot 7H_2O$), sodium hypophosphite (NaH_2PO_2) and potassium hydroxide (KOH) were purchased from Aladdin. Millipore deionized water (18.2 MΩ·cm) was used for solution preparation. Carbon cloth (WOS 1002) was obtained from CeTech, Taiwan. All the reagents used in the experiments were of analytical grade and used without further purification.

Synthesis of Co-ZIF-L/CC.[34] 2- mIm (0.165 g) and $Co(NO_3)_2 \cdot 6H_2O$ (0.116 g) were mixed in aqueous solution (10 mL) at room temperature. In this solution, a piece of CC (0.5×1.5 cm^2) repeatedly rinsed in ultrasonic cleaner with acetone, MilliQ water and absolute ethanol was vertically immersed. After static reaction for 60 minutes at room temperature, purple Co-ZIF-L deposits were obtained on the immersed CC. The Co-ZIF-L/CC was taken out of the solution, rinsed with copious Milli-Q water and ethanol, and dried under ambient condition.

Synthesis of Co-Fe-LDH/CC. Co-ZIF-L/CC was immersed in aqueous solution of $FeSO_4 \cdot 7H_2O$ (100 mM) solution to allow the reaction to realize. The

product was collected, washed with anhydrous ethanol, and dried at 60 °C overnight.

Synthesis of Co-Fe-P/CC. To achieve phosphorization, Co-Fe-LDH/CC and NaH_2PO_2 were placed at two separate positions in a closed porcelain crucible in a furnace, and NaH_2PO_2 at the upstream side of the furnace. The samples were heated under argon atmosphere to 350 °C at a ramp rate of 5 °C min^{-1} and kept at 350 °C for 3 h.

Synthesis of Co-P/CC and Fe-P/CC. The methods of synthesizing Co-P/CC and Fe-P/CC were similar to that of Co-Fe-P/CC except that the $FeSO_4 \cdot 7H_2O$ and $Co(NO_3)_2 \cdot 6H_2O$ were used instead of $CoSO_4 \cdot 7H_2O$ and into $FeSO_4 \cdot 7H_2O$, respectively.[47]

Characterization. The morphologies of all samples were examined with a field emission scanning electron microscope (FE-SEM, Hitachi, SU8010) operated at 1 kV and 10 μA. Transmission electron microscopy (TEM) images, selected-area electron diffraction (SAED) patterns and energy dispersive X-ray spectroscopy (EDX) data were recorded with a JEM-ARM200P TEM operated at 200 kV. The powder X-ray diffraction (PXRD) patterns were collected with a Rigaku MiniFlex 600 X-ray diffractometer (Cu *K*α). X-ray photoelectron spectroscopy (XPS) analysis were carried out with a Thermo ESCALAB 250XI X-ray photoelectron spectrometer. All XPS spectra were corrected against C 1s peak at 284.8 eV and the experimental data were fitted using XPS peak 4.1 software.

Electrochemical Measurements. Electrochemical measurements were performed at room temperature (25 °C) using Metrohm Autolab electrochemical workstation with a three-electrode setup, in which carbon rod was used as the counter electrode and Hg/HgO as the reference electrode. All the measurements were performed in 1.0 M KOH solution (pH = 14) that purged with O_2 prior to the OER (oxygen evolution reaction) test. Polarization data were collected at a sweep rate of 5 mV s^{-1}. Electrochemical impedance spectroscopy (EIS) measurements were carried out by applying an AC voltage with 5 mV amplitude in the frequency range from 100 kHz to 10 mHz at a potential of 1.47 V vs. RHE in 1 M KOH solution for OER. The potentials in our work were all transferred to RHE based on the equation given by

$E_{vs.RHE} = E_{vs.Hg/HgO} + 0.059\ pH + 0.098\ V = E_{vs.Hg/HgO} + 0.924\ V.$

All the LSV data were calibrated with 90% *iR* compensation.

As for powder catalyst, RuO_2 were coated on a glassy carbon electrode (GCE; working electrode). The catalyst powder (5 mg) was dispersed in solution containing Nafion solution (20 μL) and water–ethanol mixed solvent (1 mL, *v/v* = 1:1). The mixture was then ultrasonicated for at least 30 min to generate a homogeneous ink. Next, the dispersion (10 μL) was coated on GCE (5 mm in diameter) by dip coating. The as-prepared film was dried at room temperature.

Acknowledgements

This work was financially supported by the NSF of Guangdong Province (2021A1515010098, 2018A030313403), NSF of China (21821003, 21890380, 21720102007, 21701200), and LIRT Project of Guangdong PRTP Program (2017BT01C161).

Keywords: Metal phosphide• Oxygen evolution reaction• Synergistic effect• Nanosheet arrays• Electrocatalyst

[1] F. Dawood, M. Anda, G. M. Shafiullah, *Int. J. Hydrogen Energy* **2020**, *45*, 3847-3869.
[2] J. O. Abe, A. P. I. Popoola, E. Ajenifuja, O. M. Popoola, *Int. J. Hydrogen Energy* **2019**, *44*, 15072-15086.
[3] B. You, Y. Sun, *Acc. Chem. Res.* **2018**, *51*, 1571-1580.
[4] N. T. Suen, S. F. Hung, Q. Quan, N. Zhang, Y. J. Xu, H. M. Chen, *Chem. Soc. Rev.* **2017**, *46*, 337-365.
[5] H. Yang, X. Han, A. I. Douka, L. Huang, L. Gong, C. Xia, H. S. Park, B. Y. Xia, *Adv. Funct. Mater.* **2020**, *31*, 2007602.
[6] S. R. Ede, Z. Luo, *J. Mater. Chem. A* **2021**, *9*, 20131-20163.
[7] F. Lyu, Q. Wang, S. M. Choi, Y. Yin, *Small* **2019**, *15*, e1804201.
[8] F. Lu, M. Zhou, Y. Zhou, X. Zeng, *Small* **2017**, *13*.
[9] Y. Guo, T. Park, J. W. Yi, J. Henzie, J. Kim, Z. Wang, B. Jiang, Y. Bando, Y. Sugahara, J. Tang, Y. Yamauchi, *Adv. Mater.* **2019**, *31*, e1807134.
[10] Z. P. Wu, X. F. Lu, S. Q. Zang, X. W. Lou, *Adv. Funct. Mater.* **2020**, *30*, 1910274.
[11] J. Joo, T. Kim, J. Lee, S. I. Choi, K. Lee, *Adv. Mater.* **2019**, *31*, e1806682.
[12] Z. Pu, T. Liu, I. S. Amiinu, R. Cheng, P. Wang, C. Zhang, P. Ji, W. Hu, J. Liu, S. Mu, *Adv. Funct. Mater.* **2020**, *30*, 2004009.
[13] J. Su, J. Zhou, L. Wang, C. Liu, Y. Chen, *Sci. Bull.* **2017**, *62*, 633-644.
[14] H. Zhang, A. W. Maijenburg, X. Li, S. L. Schweizer, R. B. Wehrspohn, *Adv. Funct. Mater.* **2020**, *30*, 2003261.
[15] Y. Shi, B. Zhang, *Dalton. Trans.* **2017**, *46*, 16770-16773.
[16] J. Ying, H. Wang, *Front. Chem.* **2021**, *9*, 700020.
[17] Q. Shi, S. Fu, C. Zhu, J. Song, D. Du, Y. Lin, *Mater. Horiz.* **2019**, *6*, 684-702.
[18] W. Huang, J. Tang, F. Diao, C. Engelbrekt, J. Ulstrup, X. Xiao, K. Mølhave, *ChemElectroChem* **2020**, *7*, 4695-4712.
[19] S. Li, Y. Gao, N. Li, L. Ge, X. Bu, P. Feng, *Energy Environ. Sci.* **2021**, *14*, 1897-1927.
[20] Z. Li, R. Gao, M. Feng, Y. P. Deng, D. Xiao, Y. Zheng, Z. Zhao, D. Luo, Y. Liu, Z. Zhang, D. Wang, Q. Li, H. Li, X. Wang, Z. Chen, *Adv. Energy Mater.* **2021**, *11*, 2003291.
[21] B. Zhang, Y. Zheng, T. Ma, C. Yang, Y. Peng, Z. Zhou, M. Zhou, S. Li, Y. Wang, C. Cheng, *Adv. Mater.* **2021**, *33*, e2006042.
[22] T. Zhang, J. Du, P. Xi, C. Xu, *ACS Appl. Mater. Interfaces* **2017**, *9*, 362-370.
[23] R. Li, Y. Guo, H. Chen, K. Wang, R. Tan, B. Long, Y. Tong, P. Tsiakaras, S. Song, Y. Wang, *ACS Sustainable Chem. Eng.* **2019**, *7*, 11901-11910.
[24] S. J. Huang, A. Muneeb, P. Sabhapathy, A. Sheelam, K. S. Bayikadi, R. Sankar, *Dalton. Trans.* **2021**, *50*, 7212-7222.
[25] S. Song, J. Sun, J. Zhou, Z. Hu, H.-J. Lin, T.-S. Chan, C.-T. Chen, N. Zhang, C. Jing, J. Hu, L. Zhang, J.-Q. Wang, *Chem. Eng. J.* **2021**, *425*, 130681.
[26] H. Zou, X. Liu, K. Wang, Y. Duan, C. Wang, B. Zhang, K. Zhou, D. Yu, L. Y. Gan, X. Zhou, *Chem. Commun.* **2021**, *57*, 8011-8014.
[27] J. Li, D. Chu, H. Dong, D. R. Baker, R. Jiang, *J. Am. Chem. Soc.* **2020**, *142*, 50-54.
[28] A. Moysiadou, S. Lee, C. S. Hsu, H. M. Chen, X. Hu, *J. Am. Chem. Soc.* **2020**, *142*, 11901-11914.
[29] R. G. Hadt, D. Hayes, C. N. Brodsky, A. M. Ullman, D. M. Casa, M. H. Upton, D. G. Nocera, L. X. Chen, *J. Am. Chem. Soc.* **2016**, *138*, 11017-11030.
[30] Q. Chen, Q. Zhang, H. Liu, J. Liang, W. Peng, Y. Li, F. Zhang, X. Fan, *Small* **2021**, *17*, e2007858.
[31] Z. Niu, C. Qiu, J. Jiang, L. Ai, *ACS Sustainable Chem. Eng.* **2018**, *7*, 2335-2342.
[32] B. Zhang, L. Wang, Z. Cao, S. M. Kozlov, F. P. García de Arquer, C. T. Dinh, J. Li, Z. Wang, X. Zheng, L. Zhang, Y. Wen, O. Voznyy, R. Comin, P. De Luna, T. Regier, W. Bi, E. E. Alp, C.-W. Pao, L. Zheng, Y. Hu, Y. Ji, Y. Li, Y. Zhang, L. Cavallo, H. Peng, E. H. Sargent, *Nature Catal.* **2020**, *3*, 985-992.
[33] W. Hong, M. Kitta, Q. Xu, *Small Methods* **2018**, *2*, 1800214.
[34] M. Chen, Y. Xie, J.-X. Wu, H. Huang, J. Teng, D. Wang, Y. Fan, J.-J. Jiang, H.-P. Wang, C.-Y. Su, *J. Mater. Chem. A* **2019**, *7*, 10217-10224.
[35] B. Zhang, Z. Qi, Z. Wu, Y. H. Lui, T.-H. Kim, X. Tang, L. Zhou, W. Huang, S. Hu, *ACS Energy Lett.* **2018**, *4*, 328-336.
[36] M. Zhao, Y. Huang, Y. Peng, Z. Huang, Q. Ma, H. Zhang, *Chem. Soc. Rev.* **2018**, *47*, 6267-6295.

[37] W. Guo, Z. Liang, J. Zhao, B. Zhu, K. Cai, R. Zou, Q. Xu, *Small Methods* **2018**, *2*, 1800204.
[38] X. Xu, Z. Zhong, X. Yan, L. Kang, J. Yao, *J. Mater. Chem. A* **2018**, *6*, 5999-6006.
[39] J. Zhao, Y. Xie, W. Yuan, D. Li, S. Liu, B. Zheng, W. Hou, *J. Mater. Chem. B* **2013**, *1*, 1263-1269.
[40] M. Cai, Q. Liu, Z. Xue, Y. Li, Y. Fan, A. Huang, M.-R. Li, M. Croft, T. A. Tyson, Z. Ke, G. Li, *J. Mater. Chem. A* **2020**, *8*, 190-195.
[41] P. Yan, Y. Hu, E. Shoko, T. T. Isimjan, J. Tian, X. Yang, *Adv. Mater. Interfaces* **2021**, *8*, 2100065.
[42] Y. N. Wang, Z. J. Yang, D. H. Yang, L. Zhao, X. R. Shi, G. Yang, B. H. Han, *ACS Appl. Mater. Interfaces* **2021**, *13*, 8832-8843.
[43] K. Liu, C. Zhang, Y. Sun, G. Zhang, X. Shen, F. Zou, H. Zhang, Z. Wu, E. C. Wegener, C. J. Taubert, J. T. Miller, Z. Peng, Y. Zhu, *ACS Nano* **2018**, *12*, 158-167.
[44] X. Zhang, X. Zhang, H. Xu, Z. Wu, H. Wang, Y. Liang, *Adv. Funct. Mater.* **2017**, *27*, 1606635.
[45] J. Chen, Y. Zhang, H. Ye, J.-Q. Xie, Y. Li, C. Yan, R. Sun, C.-P. Wong, *ACS Appl. Energy Mater.* **2019**, *2*, 2734-2742.
[46] E. Hu, J. Ning, D. Zhao, C. Xu, Y. Lin, Y. Zhong, Z. Zhang, Y. Wang, Y. Hu, *Small* **2018**, *14*, e1704233.
[47] C. Chen, D. Xiong, M. Gu, C. Lu, F. Y. Yi, X. Ma, *ACS Appl. Mater. Interfaces* **2020**, *12*, 35365-35374.

Table of Contents

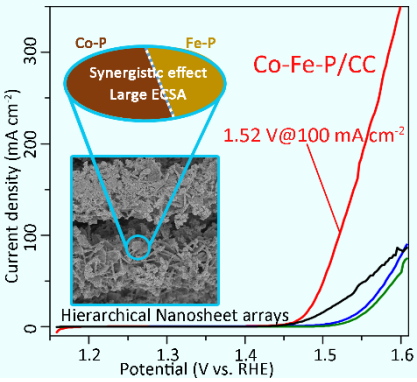

Bimetallic Co-Fe-P nanosheet arrays are developed as synergistic and highly efficient electrocatalyst for oxygen evolution reaction (OER). The Co-Fe-P electrocatalyst features pronounced synergistic effect and large electrochemical active surface area, which facilitates the generation of abundant and efficiently exposed Co^{3+} sites and thus enables the Co-Fe-P electrocatalyst to deliver excellent activity.